Iterative reflectivity-constrained velocity estimation for seismic imaging

Masaya, Shogo; Eric Verschuur, D. J.

DOI
10.1093/gji/ggy105

Publication date
2018

Document Version
Final published version

Published in
Geophysical Journal International

Geophysical Journal International

Geophys. J. Int. (2018) **214,** 1–13
Advance Access publication 2018 March 16
GJI Marine geosciences and applied geophysics

doi: 10.1093/gji/ggy105

Iterative reflectivity-constrained velocity estimation for seismic imaging

Shogo Masaya and D. J. (Eric) Verschuur

Faculty of Applied Sciences, Delft University of Technology, Lorentzweg 1, 2628 *CJ, Delft, the Netherlands. E-mail: masayaka9u5@gmail.com*

Accepted 2018 March 15. Received 2017 November 9; in original form 2017 May 26

SUMMARY

This paper proposes a reflectivity constraint for velocity estimation to optimally solve the inverse problem for active seismic imaging. This constraint is based on the velocity model derived from the definition of reflectivity and acoustic impedance. The constraint does not require any prior information of the subsurface and large extra computational costs, like the calculation of so-called Hessian matrices. We incorporate this constraint into the joint migration inversion algorithm, which simultaneously estimates both the reflectivity and velocity model of the subsurface in an iterative process. Using so-called full wavefield modelling, the misfit between forward modelled and measured data is minimized. Numerical and field data examples are given to demonstrate the validity of our proposed algorithm in case accurate initial models and the low-frequency components of observed seismic data are absent.

Key words: Image processing; Inverse theory; Waveform inversion; Seismic tomography.

1 INTRODUCTION

A fundamental problem in active seismic imaging is that both the depth reflectivity and velocity distribution of the subsurface have to be predicted by only seismic events observed at the surface, which is a mathematically ill-posed problem. Two types of approaches have been mainly utilized for addressing this problem in the oil and gas industry. One approach consists of solving the problems in two separate steps: velocity estimation and migration. In this approach, migration provides the reflectivity image based on the typically smooth velocity model provided by a preceding velocity estimation method, like full waveform inversion (FWI) (Tarantola 1984; Virieux & Operto 2009). Another approach is to utilize an interactive procedure between velocity and reflectivity estimation. For example, migration velocity analysis (MVA) (Liu & Bleistein 1995) has been commonly used as this approach.

FWI enables us to estimate a high-resolution velocity model through matching a forward modelled response with the events of observed 'waveform' data (presented by Tarantola 1984), which correspond to so-called diving waves in the standard FWI algorithm for seismic data. However, as FWI is a strongly non-linear inverse problem, the solutions tend to converge to local minima, which mean inaccurate velocity models. It is known that several conditions such as correctness of the initial velocity and presence of low-frequency components of the observed data are crucial in preventing the local minima in FWI (see, e.g. Virieux & Operto 2009). Several approaches have been proposed to mitigate the local minima with the reduced conditions. For example, the effectiveness of a misfit criterion via Wiener filters for the observed data for FWI was demonstrated in Warner & Guasch (2016), and a penalty method for partial differential equation constraint was also applied to diminish the conditions in van Leeuwen & Herrmann (2016). In relation to the local minima problem, reconstructing the velocity for high-contrast geobodies (e.g. salt, basalt) is still a challenge in FWI. In Esser *et al.* (2015), an approach was introduced based on total variation and Hinge loss used in support vector machine, which is an algorithm of machine learning, to realize the estimation for a high-contrast velocity model. This approach was expanded by the split Bregman method (Goldstein & Osher 2009), although these approaches require the prior information for true total variation and Hinge loss of the subsurface (Qiu *et al.* 2016). In addition to the challenge caused by the local minima, data acquisition with long offsets is indispensable to obtain enough depth penetration because standard FWI exploits diving waves. As stated, since FWI is the first process in the two steps-based approach, migration has to be applied by using the velocity predicted by FWI.

MVA is capable of stably updating the velocity distribution by improving the flatness of so-called common image gathers, which are the migrated images with the previous velocity, in the offset or angle domain (Biondi & Symes 2004; Sava & Biondi 2004). Although the velocity updated via MVA takes into account information on the reflectivity of the migrated image, a more advanced migration scheme, like reverse time migration (RTM), is often applied for finally using the predicted velocity after MVA. Thus, the approach based on MVA also requires an additional migration process to give the final image as the second step.

Joint migration inversion (JMI) was proposed as one of the methods to simultaneously estimate both velocity and depth reflectivity distributions and to reduce the mentioned non-linearity in FWI (Berkhout 2012, 2014b). This means that the two steps containing

velocity analysis and migration are integrated in the JMI process. The seismic modelling algorithm in the JMI process is so-called full wavefield modelling (FWMod) (Berkhout & Verschuur 2011; Berkhout 2014a), which is a reflection modelling process, including higher order scattering and transmission effects, with similarities to the Bremmer series in optics (Bremmer 1951). This means that the JMI process utilizes internal multiples for the imaging, although conventional imaging methods such as MVA, standard RTM and standard FWI, do not deal with internal multiples. In the data modelling procedure, the velocity model only affects the kinematics without any scattering effect in the modelling operators and the reflectivity model only deals with scattering effects. Hence, due to the involved decoupling of the parameters reflectivity and velocity, the inverse problem becomes less non-linear. However, for accurate inversion, when searching the global minimum, some coupling between the two types of parameters will be desired in the end. In this paper, we discuss the velocity estimation imposed on a reflectivity constraint to accurately solve this inverse problem.

Several prior studies reported that reflectivity information can aid the optimization of velocity inversion. Although MVA might be also categorized in such approach, the drawback of MVA is that the resolution of the updated velocity is relatively low because MVA exploits the flatness of common image gathers instead of fitting modelled with measured data. A scheme to combine MVA with FWI was also suggested in Biondi & Almomin (2012) to improve the resolution. Incorporating the information of migration into the tomography process for velocity estimation improves the final depth image (Mathewson *et al.* 2012), where a dirty salt velocity was estimated via the reflectivity, which is computed by true-amplitude RTM, under a 1D assumption (Ji *et al.* 2011). With a similar reasoning, Maciel *et al.* (2015) applied nonlinear filters from the field of morphological image processing to address this challenge and to enhance the contrast of the JMI velocity solution. In order to improve the resolution of the velocity model, we also presented an initial algorithm and result (Masaya & Verschuur 2016) for reflectivity-constrained velocity estimation by adding a slowness-based objective function in JMI, which independently inverts reflectivity and velocity models.

In this paper, we propose a new reflectivity-based objective function instead of the mentioned slowness-based objective function for the reflectivity-constrained velocity estimation in JMI. The objective function per iteration is based on the difference between the estimated reflectivity from JMI and the reflectivity approximated from the estimated velocity from JMI. In addition, a sparsity constraint for the reflectivity estimation is introduced to promote the effect of the reflectivity-constrained velocity estimation. We call this algorithm reflectivity-constrained JMI (RCJMI) in this paper. RCJMI aims to automatically update velocity with this reflectivity constraint and also reflectivity in an alternating iteration process.

This paper first describes notations and the review of JMI in Section 2 and, next, gives an algorithm for our proposed reflectivity-constrained velocity estimation in Section 3. Then, synthetic and field data examples are presented in Section 4. The extension to mitigate the assumption in the proposed algorithm is mainly discussed in Section 5. Finally, we draw conclusions on the basis of the results for the examples in Section 6.

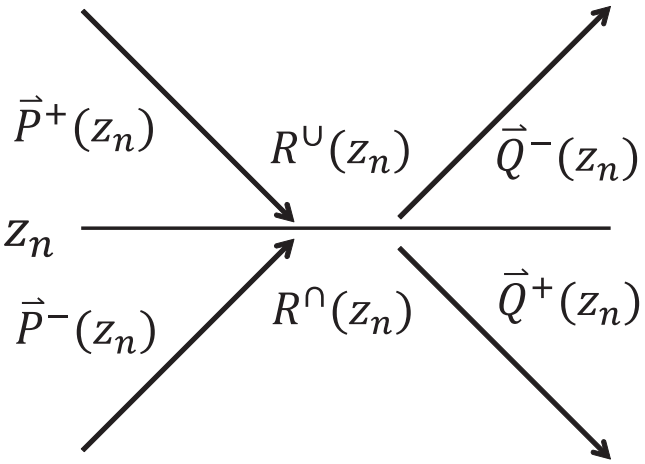

Figure 1. Reflected and transmitted wavefields at depth level z_n.

2 NOTATIONS AND REVIEW

We consider a 2D seismic data with $N_r \in \mathbb{N}^+$ receivers, $N_s \in \mathbb{N}^+$ sources and $N_\omega \in \mathbb{N}^+$ frequency samples. Since a so-called staggered grid is utilized to describe the grid of the subsurface, the reflectivity model and P-wave velocity model are defined by $\mathbf{m_r} \in \mathbb{R}^{(M+1)\times N_x}$ and $\mathbf{m_c} \in \mathbb{R}^{>0, M\times N_x}$ with $N_x \in \mathbb{N}^+$ lateral samples and $M \in \mathbb{N}^+$ depth samples. The elements of the reflectivity and velocity model at a lateral location x and depth z are written by $r(x, z)$ and $c(x, z)$, respectively.

Let $\mathsf{P}^{\pm}(z_n) \in \mathbb{C}^{N_r\times N_s\times N_\omega}$ and $\mathsf{W}^{\pm}(z_{n\pm1}; z_n) \in \mathbb{C}^{N_r\times N_r\times N_\omega}$ be the downgoing/upgoing wavefields at depth level z_n and the downgoing/upgoing propagation operators between z_n and $z_{n\pm1}$ in the frequency domain, respectively. Here, the signs, $^{*+}$ and $^{*-}$, represent 'downgoing' and 'upgoing'. Let $\mathbf{R}^{\cup}(z_n), \mathbf{R}^{\cap}(z_n) \in \mathbb{R}^{N_r\times N_r}$ be reflection operators at z_n, as illustrated in Fig. 1. When we consider a monochromatic wavefield with the frequency $\omega_f, f = 1, 2, \cdots, N_\omega$, and the source located at $x_{s,\xi}, \xi = 1, 2, \cdots, N_s$, the downgoing/upgoing wavefields are written by $\vec{P}^{\pm}(z_n, x_{s,\xi}, \omega_f) \in \mathbb{C}^{N_r}$, which are the vectors in $\mathsf{P}^{\pm}(z_n)$. The propagation operator at the frequency ω_f is also described by $\mathbf{W}^{\pm}(z_{n\pm1}; z_n, \omega_f) \in \mathbb{C}^{N_r\times N_r}$, which is the matrices in $\mathsf{W}^{\pm}(z_{n\pm1}; z_n)$. For the simplification, we use the following notations (e.g. see Berkhout 1982) for monochromatic wavefields and propagation operators:

$$\vec{P}^{\pm}(z_n) \equiv \vec{P}^{\pm}(z_n, x_{s,\xi}, \omega_f), \tag{1}$$

$$\mathbf{W}^{\pm}(z_{n\pm1}; z_n) \equiv \mathbf{W}^{\pm}(z_{n\pm1}; z_n, \omega_f). \tag{2}$$

Note that although we describe and demonstrate the process for the 2D case, the method can easily be extended to the full 3D situation (such as described in Kinneging *et al.* 1989; Davydenko & Verschuur 2017).

2.1 Representations for reflection, transmission and propagation

This subsection reviews the representation for the reflection, transmission and propagation to introduce our discussed inverse problem. When a monochromatic downgoing wavefield $\vec{P}^{+}(z_n)$ at depth level z_n is reflected at a sharp discontinuity, we can write the reflected wavefield in the frequency domain by using a reflection operator

$\mathbf{R}^{\cup}(z_n)$:

$$\vec{Q}^{-}(z_n) = \mathbf{R}^{\cup}(z_n)\vec{P}^{+}(z_n). \tag{3}$$

Since the upgoing wavefield does not contain only energy from the reflected wavefield but also from the transmitted wavefield in the discontinuity, at depth level z_n, we can actually express:

$$\vec{Q}^{-}(z_n) = \mathbf{T}^{-}(z_n)\vec{P}^{-}(z_n) + \mathbf{R}^{\cup}(z_n)\vec{P}^{+}(z_n), \tag{4}$$

where $\vec{Q}^{-}(z_n) \in \mathbb{C}^{N_r}$ indicates the total upgoing wavefield moving away from the discontinuity, $\vec{P}^{-}(z_n)$ describes the upgoing incoming wavefield at depth level z_n from below, and $\mathbf{T}^{-}(z_n)$ represents a transmission operator in the discontinuity (see Fig. 1). The transmission operators are defined as $\mathbf{T}^{\pm}(z_n) \equiv \mathbf{I} + \delta\mathbf{T}^{\pm}(z_n)$, meaning that differential transmission operator $\delta\mathbf{T}^{\pm}(z_n) = 0$ if there is no contrast at z_n. Then, eq. (4) is written as:

$$\vec{Q}^{-}(z_n) = \vec{P}^{-}(z_n) + \delta\mathbf{T}^{-}(z_n)\vec{P}^{-}(z_n) + \mathbf{R}^{\cup}(z_n)\vec{P}^{+}(z_n), \tag{5}$$

where the last two terms contain the scattered wavefields at depth level z_n for the wavefields that arrive from both sides.

In a similar way, the total downgoing wavefield $\vec{Q}^{+}(z_n) \in \mathbb{C}^{N_r}$ that leaves the depth level z_n can be written as a sum of transmission and reflection terms:

$$\begin{aligned}\vec{Q}^{+}(z_n) &= \mathbf{T}^{+}(z_n)\vec{P}^{+}(z_n) + \mathbf{R}^{\cap}(z_n)\vec{P}^{-}(z_n)\\ &= \vec{P}^{+}(z_n) + \delta\mathbf{T}^{+}(z_n)\vec{P}^{+}(z_n) + \mathbf{R}^{\cap}(z_n)\vec{P}^{-}(z_n).\end{aligned} \tag{6}$$

Eqs (4)–(6) are similar to the representation of the Bremmer series (Bremmer 1951), which is exploited in the mentioned FWMod process (Berkhout & Verschuur 2011).

The wavefields $\vec{Q}^{\pm}(z_n)$ after the transmission and reflection at z_n propagate to the neighboring depth levels $z_{n\pm1}$ via the wavefield extrapolation based on the Rayleigh II integral:

$$\vec{P}^{\pm}(z_{n\pm1}) = \mathbf{W}^{\pm}(z_{n\pm1}; z_n)\vec{Q}^{\pm}(z_n), \tag{7}$$

where $\mathbf{W}^{+}(z_{n+1}; z_n)$ and $\mathbf{W}^{-}(z_{n-1}; z_n)$ are the downgoing and upgoing propagation operators to propagate the wavefields to the next depth level $z_{n\pm1}$. The elements of $\mathbf{W}$ are written by:

$$W_{i,j}(z_m; z_n) = 2\mathrm{sign}(z_n - z_m)\frac{\partial G}{\partial z}(x_j, z_m; x_i, z_n), \tag{8}$$

where $G(x_j, z_m; x_i, z_n)$ represents a Green's function from the original location (x_j, z_m) to the extrapolated wavefield location at (x_i, z_n). Within a homogeneous layer, the matrix $\mathbf{W}$ exhibits a Toeplitz structure. This means that the one-way propagation operator in the medium (i.e. one column of $\mathbf{W}$) is simply defined by a phase-shift operator (Gazdag 1978):

$$\vec{W}_j(z_m; z_n) = \mathcal{F}_x^{-1}[e^{-jk_z\Delta\tilde{z}}e^{-jk_x x_j}], \tag{9}$$

with

$$k_z = \begin{cases}\sqrt{k^2 - k_x^2}, & (|k_x| \le |k|),\\ -j\sqrt{k_x^2 - k^2}, & (|k_x| > |k|),\end{cases} \tag{10}$$

where $\Delta\tilde{z} \equiv |z_n - z_m|$ and $k \equiv \omega/c$. $\mathcal{F}_x$ is the spatial Fourier transform.

In the FWMod procedure, the scattering process described in eqs (5) and (6) and the propagation process described in eq. (7) are recursively performed at each depth. The procedure can be summarized in the following equations (Berkhout 2014a):

(i) for the downgoing wavefields ($m = 1, 2, \cdots, M$):

$$\begin{aligned}\vec{P}^{+}(z_m) &= \underline{\mathbf{W}}^{+}(z_m; z_0)\vec{S}^{+}(z_0)\\ &\quad + \sum_{n=0}^{m-1}\underline{\mathbf{W}}^{+}(z_m; z_n)\mathbf{R}^{\cap}(z_n)\vec{P}^{-}(z_n),\end{aligned} \tag{11}$$

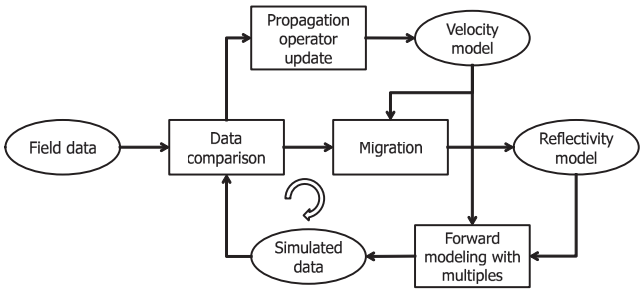

Figure 2. Flowchart of JMI.

with

$$\underline{\mathbf{W}}^{+}(z_m; z_n) \equiv \mathbf{W}^{+}(z_m; z_{m-1})\prod_{l=m-1}^{n+1}\mathbf{T}^{+}(z_l)\mathbf{W}^{+}(z_l; z_{l-1}), \tag{12}$$

(ii) for the upgoing wavefields ($m = 0, 1, \cdots, M-1$):

$$\begin{aligned}\vec{P}^{-}(z_m) &= \underline{\mathbf{W}}^{-}(z_m; z_M)\vec{P}^{-}(z_M)\\ &\quad + \sum_{n=m+1}^{M}\underline{\mathbf{W}}^{-}(z_m; z_n)\mathbf{R}^{\cup}(z_n)\vec{P}^{+}(z_n),\end{aligned} \tag{13}$$

with

$$\underline{\mathbf{W}}^{-}(z_m; z_n) \equiv \mathbf{W}^{-}(z_m; z_{m+1})\prod_{l=m+1}^{n-1}\mathbf{T}^{-}(z_l)\mathbf{W}^{-}(z_l; z_{l+1}), \tag{14}$$

where $\vec{S}^{+}(z_0)$ is a downgoing source wavefield at the surface.

2.2 Joint migration inversion

JMI is an inversion algorithm to optimize velocity and reflectivity models of the subsurface by minimizing the residual between observed and modelled data, which takes into account the scattering and propagation process based on the mentioned FWMod process, as shown in Fig. 2.

In the standard implementation for JMI (Staal & Verschuur 2013; Staal *et al.* 2014; Verschuur *et al.* 2016), the objective function, which contains the residual between the observed data and the modelled data, is defined as follows:

$$J = \frac{1}{2}\sum_{\xi}^{N_s}\sum_{f}^{N_\omega}\|\vec{P}^{-}_{obs}(z_0, x_{s,\xi}, \omega_f) - \vec{P}^{-}_{mod}(z_0, x_{s,\xi}, \omega_f)\|^2, \tag{15}$$

where $\vec{P}^{-}_{obs}(z_0, x_{s,\xi}, \omega_f)$ and $\vec{P}^{-}_{mod}(z_0, x_{s,\xi}, \omega_f)$ represent the observed shot data and forward modelled shot data, respectively. Note that this objective function takes into account multishots and multifrequency components of seismic data instead of one shot and its monochromatic component.

The reflectivity and velocity update for eq. (15) is solved by a gradient decent scheme, as shown in Algorithm 1. Here, ∇J_r and α_r represent the gradient and scale factor for the reflectivity update. ∇J_σ and α_σ are the gradient and scale factor for the slowness update. Furthermore, $*^{(k)}$ indicates kth iteration in this inversion and $*_i$ Seismic tomography.is the roundtrip number in JMI. The detailed formulation for the update rules is described in Appendix A.

On the basis of the above procedure, JMI enables to automatically update reflectivity and slowness/velocity models of the subsurface in an alternating manner in each iteration. Like typically done in FWI, to improve the convergence, the JMI process is run according to a certain frequency schedule, starting with a low-frequency range and expanding the range after certain number of iterations.

Algorithm 1 Reflectivity and velocity update process by gradient decent scheme for JMI

Input: $K \in \mathbb{N}^+$, initial guess: r^0, c^0
1: **for** $k = 1 \rightarrow K$ **do**
2: $i = 2k - 1$
3: Compute $\vec{Q}_i^{\pm}$ by equation (5) and (6)
4: Compute $\vec{P}_i^{\pm}$ by equation (11) and (13)
5: Compute ∇J_r by equation (A.4)
6: Compute α_r by equation (A.7)
7: Update $r^{(k)} = r^{(k-1)} + \alpha_r \nabla J_r$
8: $i = 2k$
9: Compute $\vec{Q}_i^{\pm}$ by equation (5) and (6)
10: Compute $\vec{P}_i^{\pm}$ by equation (11) and (13)
11: Compute ∇J_σ by equation (A.21)
12: Compute α_σ by equation (A.23)
13: Update $\sigma^{(k)} = \sigma^{(k-1)} + \alpha_\sigma \nabla J_\sigma$
14: **end for**

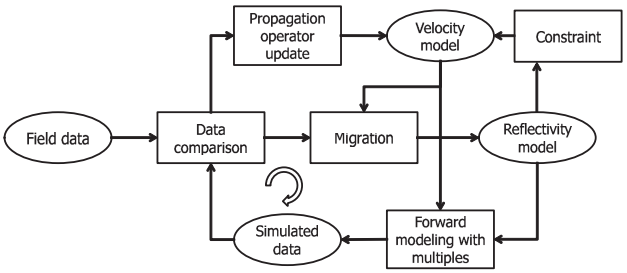

Figure 3. Overview of RCJMI, where the estimated image also constrains the velocity update.

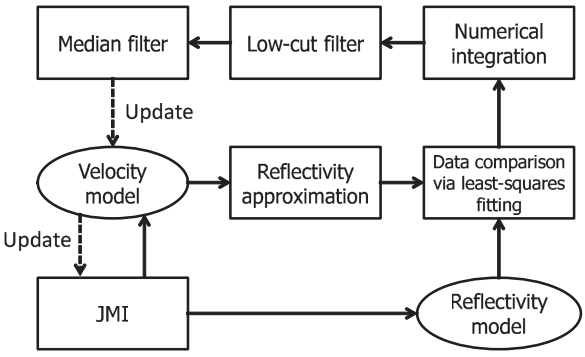

Figure 4. The scheme for the velocity update with a reflectivity-based constraint in each iteration of RCJMI. Note that the block 'JMI' refers to the process shown in Fig. 3.

3 REFLECTIVITY-CONSTRAINED VELOCITY ESTIMATION

In this section, we describe our proposed algorithm for iteratively and automatically reflectivity-constrained velocity estimation. The main idea in this algorithm is to impose a reflectivity-based constraint during the velocity estimation step to improve the accuracy of the JMI solution, as illustrated in Figs 3 and 4. Furthermore, a sparsity constraint in the reflectivity update is introduced to further enhance the reflectivity-constrained velocity estimation.

3.1 Reflectivity approximation based on velocity

First, we derive a reflectivity approximation formulated from the estimated velocity. If waves are normally incident to the boundary between depth level z_n and z_{n+1}, the reflection equation for $n = 0, \cdots, M-2$ can be described by:

$$r(x, z_{n+1}) = \frac{\rho(x, z_{n+1})c(x, z_{n+1}) - \rho(x, z_n)c(x, z_n)}{\rho(x, z_{n+1})c(x, z_{n+1}) + \rho(x, z_n)c(x, z_n)}, \tag{16}$$

where c and ρ represent the velocity and density model of the subsurface. Next, we assume for our constraint calculation that the density model ρ is constant because in general the density variation of the subsurface is relatively small compared to the velocity variation. Then, the reflectivity is approximately calculated by:

$$r(x, z_{n+1}) \simeq \frac{c(x, z_{n+1}) - c(x, z_n)}{c(x, z_{n+1}) + c(x, z_n)}. \tag{17}$$

We additionally assume that the horizontal variation of velocity models is much smaller than the vertical variation. Then, a numerical approximation can be obtained from eq. (17):

$$r(x, z_{n+1}) \sim \frac{\Delta c}{\Delta z} \times \text{const.}, \tag{18}$$

where $\Delta c \equiv c(x, z_{n+1}) - c(x, z_n)$ and $\Delta z \equiv z_{n+1} - z_n$. Eq. (18) means a relationship between reflectivity and velocity. Therefore, an estimated reflectivity r_{constr} derived from the velocity model, which does not include the scale of the correct reflectivity, can be defined by:

$$r_{\text{constr}} \equiv \frac{\partial c}{\partial z}. \tag{19}$$

3.2 Objective function

An objective function for our proposed RCJMI is defined by the mentioned reflectivity approximation based on the estimated velocity, i.e. r_{constr}, and is given as:

$$\begin{aligned} J = & \frac{1}{2} \sum_{\xi}^{N_s} \sum_{f}^{N_\omega} \| P_{\text{obs}}^{-}(z_0, x_{s,\xi}, \omega_f) - P_{\text{mod}}^{-}(z_0, x_{s,\xi}, \omega_f) \|^2 \\ & + \lambda_2 \| r(x, z) - \Lambda r_{\text{constr}}(x, z) \|_2^2 \\ & + \frac{\lambda_3}{2} \sum_{x} \sum_{z} \ln\{1 + \kappa^{-2} r^2(x, z)\}, \end{aligned} \tag{20}$$

where $\lambda_2, \lambda_3 \in \mathbb{R}^+$ represent the weight parameters for the second and third terms, respectively. $\Lambda \in \mathbb{R}^+$ represents a scale factor between $r(x, z)$ and $r_{\text{constr}}(x, z)$ that also takes care of the difference in units. $\kappa \in \mathbb{R}^+$ indicates a parameter controlling the sparseness of the reflectivity. We express separately the three terms in the RHS of eq. (20):

$$J_1 \equiv \tfrac{1}{2} \textstyle\sum_{\xi}^{N_s} \sum_{f}^{N_\omega} \| P_{\text{obs}}^{-}(z_0, x_{s,\xi}, \omega_f) - P_{\text{mod}}^{-}(z_0, x_{s,\xi}, \omega_f) \|^2, \tag{21}$$

$$J_2 \equiv \lambda_2 \| r(x, z) - \Lambda r_{\text{constr}}(x, z) \|_2^2, \tag{22}$$

$$J_3 \equiv \tfrac{\lambda_3}{2} \textstyle\sum_{x} \sum_{z} \ln\{1 + \kappa^{-2} r^2(x, z)\}, \tag{23}$$

where J_1 is the standard misfit term that is also described in eq. (15). J_2 is a term of the reflectivity constraint to minimize the residual between the reflectivity calculated by JMI and the reflectivity approximated by the estimated velocity from JMI. J_3 is an optional term to enhance the sparseness of the reflectivity (Sacchi *et al.* 1998). As

for the weight parameter (λ_2) and sparsity parameter (λ_3) in RCJMI, the optimum values are determined via several parameter tests in each example. Note that if λ_2 is chosen too large, velocity updates will be calculated almost exclusively from the integrated reflectivity values. On the other hand, if λ_2 and λ_3 are chosen too small, the velocity and reflectivity updates will be mainly determined by the data misfit term.

3.3 Reflectivity and velocity updates

As stated previously, the update procedure in JMI consists of the reflectivity and slowness/velocity updates, which are derived from the gradient decent scheme. In RCJMI, the standard misfit function described by J_1 of eq. (21) and the sparsity function described by J_3 of eq. (23) are used for the reflectivity update. On the other hand, the velocity update in RCJMI is based on the standard misfit function shown in J_1 of eq. (21) and the reflectivity-constraint function expressed by J_2 of eq. (22).

The gradient of J_3 for the reflectivity update is simply calculated by:

$$\nabla J_{3,r}(x,z) = \lambda_3 \frac{r(x,z)}{\kappa^2 + r^2(x,z)}. \tag{24}$$

Therefore, the following reflectivity update for RCJMI is given by:

$$r^{(k+1)}(x,z) = r^{(k)}(x,z) + \alpha_r(\nabla J_{1,r}(x,z) + \nabla J_{3,r}(x,z)). \tag{25}$$

As for the velocity update in RCJMI, since the approximated reflectivity $r_{\text{constr}}(x, z)$ does not have a correct scale, the reflectivity residual $r_{\text{res}}(x, z)$ between $r(x, z)$ and $r_{\text{constr}}(x, z)$ is computed via least-squares fitting in the first step (see Fig. 4):

$$r_{\text{res}}(x,z) \equiv r(x,z) - \Lambda r_{\text{constr}}(x,z), \tag{26}$$

$$\Lambda = \arg\min_{\Lambda} \|r(x,z) - \Lambda r_{\text{constr}}(x,z)\|_2^2. \tag{27}$$

To obtain the gradient of J_2 for the velocity update, we take the numerical integral of the reflectivity residual $r_{\text{res}}(x, z)$ along z:

$$\nabla J_{2,c}(x,z) = \lambda_2 \int_{z_0}^{z} r_{\text{res}}(x,z')dz'. \tag{28}$$

We apply a low-cut filter and a horizontal median filter to the gradient $\nabla J_{2,c}(x, z)$. The low-cut filter applied to the gradient $\nabla J_{2,c}(x, z)$ along z is used to provide a sharp velocity update. After the application of the low-cut filter, a horizontal median filter for the gradient is performed to remove the outliers, which can generate artefacts.

A scale factor for the velocity update of this term is given by:

$$\alpha_{c2} = \frac{\sum_x \sum_z |\int_{z_0}^{z} r_{res}(x,z')dz'|^2}{\sum_x \sum_z |\int_{z_0}^{z} r(x,z')dz'|^2}. \tag{29}$$

Therefore, we can update the velocity model as follows:

$$c^{(k+1)}(x,z) = \frac{1}{\sigma^{(k)}(x,z) + \alpha_{\sigma 1}\nabla J_{1,\sigma}(x,z)} + \alpha_{c2}\nabla J_{2,c}(x,z), \tag{30}$$

where $\nabla J_{1,\sigma}$ and $\alpha_{\sigma 1}$ are the gradient and scale factor of the slowness $\sigma(= 1/c)$ in standard JMI, which correspond to ∇J_σ of eq. (A21) and α_σ of eq. (A23) in Appendix A. The reflectivity and velocity update procedure in RCJMI is summarized in Algorithm 2.

Algorithm 2 Reflectivity and velocity update process in RCJMI

Input: $K \in \mathbb{N}^+$, initial guess: r^0, c^0
for $k = 1 \rightarrow K$ **do**
  $i = 2k - 1$
  Compute $\vec{Q}_i^{\pm}$ by equation (5) and (6)
  Compute $\vec{P}_i^{\pm}$ by equation (11) and (13)
  Compute $\nabla J_{1,r}$ by equation (A.4)
  Compute $\nabla J_{3,r}$ by equation (24)
  Compute α_r by equation (A.7)
  Update $r^{(k)} = r^{(k-1)} + \alpha_r(\nabla J_{1,r} + \nabla J_{3,r})$
  $i = 2k$
  Compute $\vec{Q}_i^{\pm}$ by equation (5) and (6)
  Compute $\vec{P}_i^{\pm}$ by equation (11) and (13)
  Compute $\nabla J_{1,\sigma}$ by equation (A.21)
  Compute $\nabla J_{2,c}$ by equation (28)
  Apply low-cut filter and median filter to $\nabla J_{2,c}$
  Compute $\alpha_{\sigma 1}$ by equation (A.23)
  Compute α_{c2} by equation (29)
  Update $c^{(k)} = 1/(\sigma^{(k-1)} + \alpha_{\sigma 1}\nabla J_{1,\sigma}) + \alpha_{c2}\nabla J_{2,c}$
  Compute $\sigma^{(k)} = 1/c^{(k)}$
end for

4 RESULTS

This section provides two synthetic data examples and one field data example to evaluate the effectiveness of RCJMI in comparison with standard JMI. Shot data for the synthetic examples is generated by FWMod with a Ricker source wavelet centered at 20 Hz in order to correctly examine the effect of our proposed constraints. Up to the fifth order of multiples are included in the synthetic data. The acquisition in the synthetic examples assumes to use fixed receivers at the top of the depth level ($z = 0$).

4.1 Lens-shaped model

The first example is a 2D model containing a lense-shaped anomaly, shown in Figs 5(a) and (b). The model consists of the high-velocity region with a lense shape and three horizontal reflectors under the region. The receiver and source intervals are 20 and 80 m, respectively.

Three frequency schedules, as shown in Tables 1–3, for the iteration of the inversions are tested to investigate the frequency dependence with the same conditions aside from the schedule. The maximum offset in the data used for the inversion is 2000 m. Figs 5(c) and (d) show the initial velocity and reflectivity models for the inversions. The parameters $\lambda_2 = 15$, $\lambda_3 = 5.0 \times 10^{-7}$, and $\kappa = 2.5 \times 10^{-2}$ are used for RCJMI.

Figs 5(e)–(l) represent the results of JMI and RCJMI with frequency schedule I. It can be seen that RCJMI accurately inverts a velocity field and, as a result, the reflectivity image is also correctly migrated (see Figs 5k and l). On the other hand, Figs 6(a)–(h) and 7(a)–(d) indicate the results of JMI and RCJMI with frequency schedule II and III, respectively. As shown in Figs 5(f) and (j), the velocity profiles given by JMI apparently include the artefacts beneath the high-velocity region, while these are almost absent in Figs 6(b) and (f) and 7(b). This means that the accuracy of the models estimated by JMI strongly depends on each frequency schedule. However, RCJMI is capable of providing highly accurate velocity and reflectivity models, as illustrated in Fig. 8.

To quantitatively evaluate the accuracy of the velocity estimation for JMI and RCJMI, the following velocity error c_{error} is defined:

$$c_{\text{error}} \equiv \frac{\sum_x \sum_z |c_{\text{true}}(x,z) - c_{\text{est}}(x,z)|}{\sum_x \sum_z c_{\text{true}}(x,z)}, \tag{31}$$

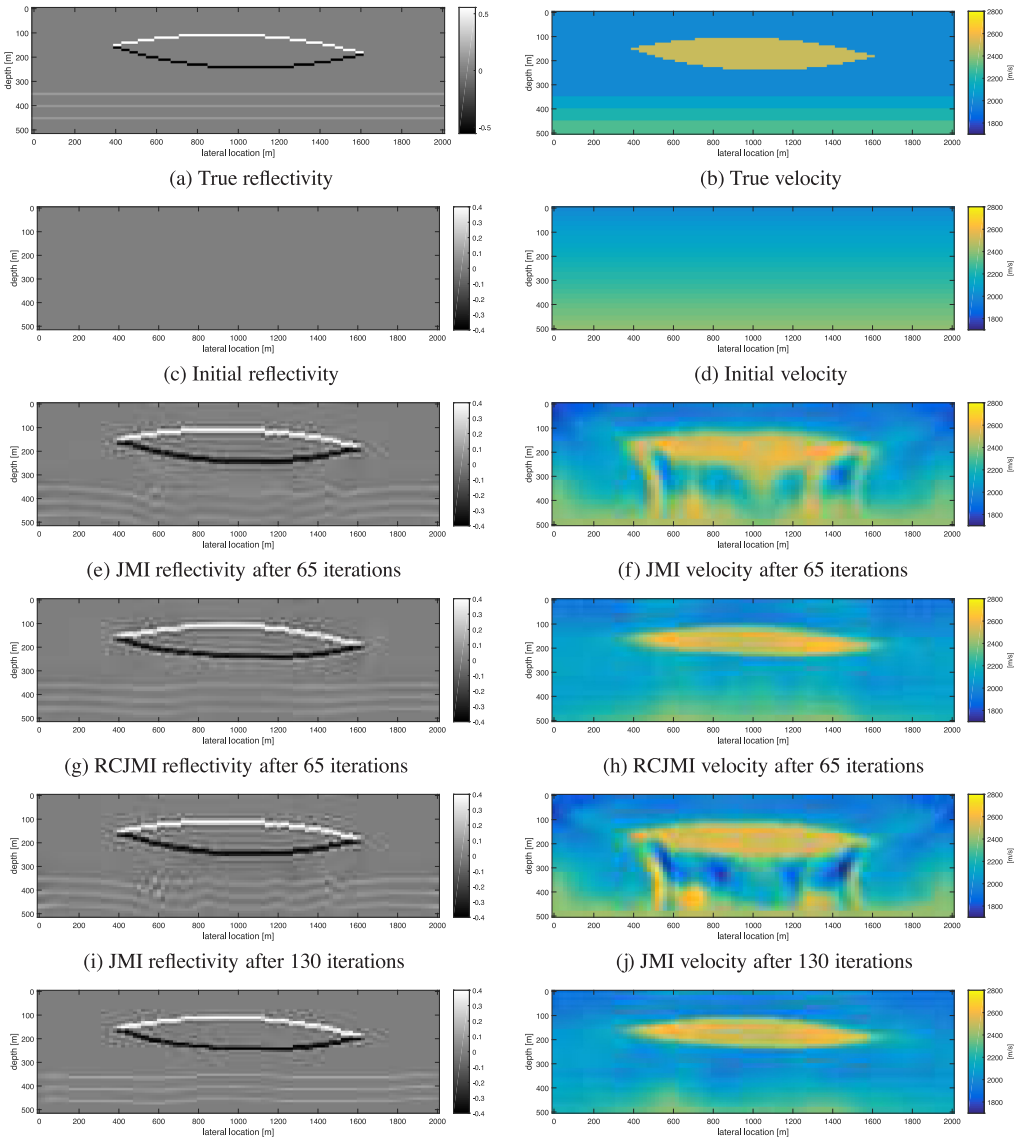

(a) True reflectivity (b) True velocity

(c) Initial reflectivity (d) Initial velocity

(e) JMI reflectivity after 65 iterations (f) JMI velocity after 65 iterations

(g) RCJMI reflectivity after 65 iterations (h) RCJMI velocity after 65 iterations

(i) JMI reflectivity after 130 iterations (j) JMI velocity after 130 iterations

(k) RCJMI reflectivity after 130 iterations (l) RCJMI velocity after 130 iterations

Figure 5. Reflectivity and velocity models in the first example with frequency schedule I (5–40 Hz). It can be seen that RCJMI stably provides accurate velocity models, while the velocity models estimated by JMI include artefacts.

Table 1. The frequency schedule I for JMI and RCJMI in the first example.

Order	Frequency (Hz)	No. of iterations
1	5–10	12
2	5–20	12
3	5–30	10
4	5–40	106
		Total 140

Table 2. The frequency schedule II for JMI and RCJMI in the first example.

Order	Frequency (Hz)	No. of iterations
1	5–10	5
2	5–20	15
3	5–30	15
4	5–40	105
		Total 140

Table 3. The frequency schedule III for JMI and RCJMI in the first example.

Order	Frequency (Hz)	No. of iterations
1	10–15	5
2	10–23	15
3	10–32	15
4	10–40	105
		Total 140

where c_{true} and c_{est} are the true velocity and the velocity estimated by the inversions. Fig. 9 shows the iteration dependence of the velocity error c_{error} for JMI and RCJMI using frequency schedules I, II and III. It is clear that the performance of RCJMI is not sensitive to the frequency schedule, although the solutions inverted by JMI relatively converge to local minima. Note again that we are dealing with a so-called 'inverse crime', where the same FWMod is used to obtain the shot data. Thus, in theory a perfect inversion result

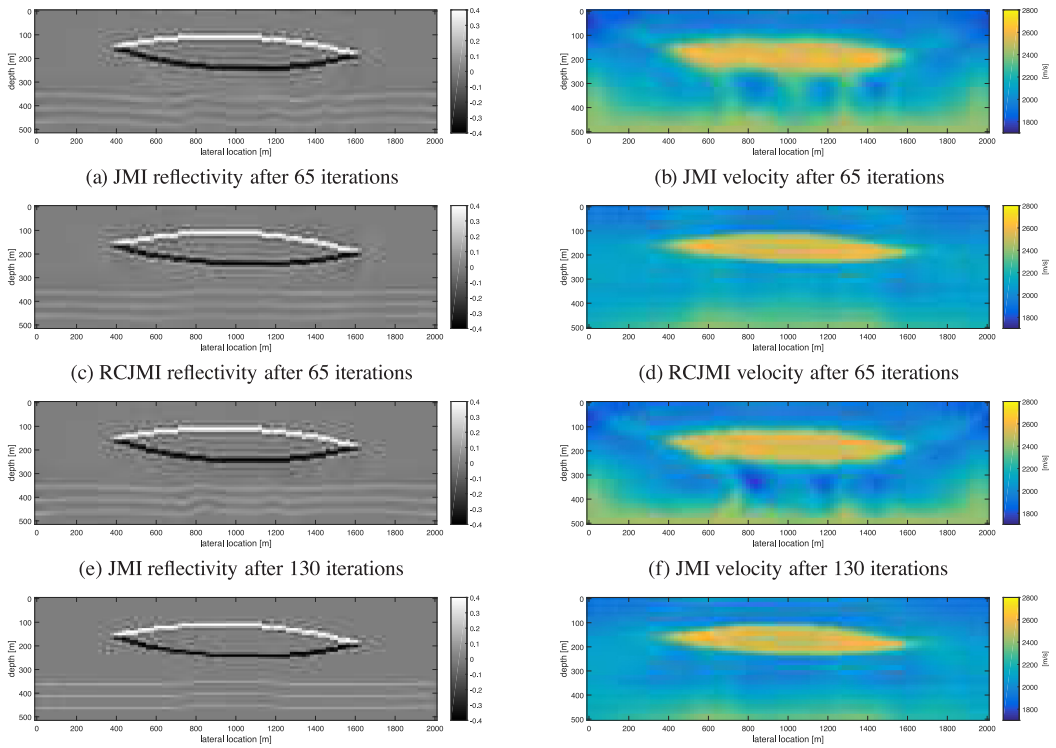

(a) JMI reflectivity after 65 iterations
(b) JMI velocity after 65 iterations
(c) RCJMI reflectivity after 65 iterations
(d) RCJMI velocity after 65 iterations
(e) JMI reflectivity after 130 iterations
(f) JMI velocity after 130 iterations
(g) RCJMI reflectivity after 130 iterations
(h) RCJMI velocity after 130 iterations

Figure 6. Estimated reflectivity and velocity models for the first example with frequency schedule II (5–40 Hz). Note that with this frequency schedule JMI results are better, although the final RCJMI results are similar to that of schedule I (Fig. 5)

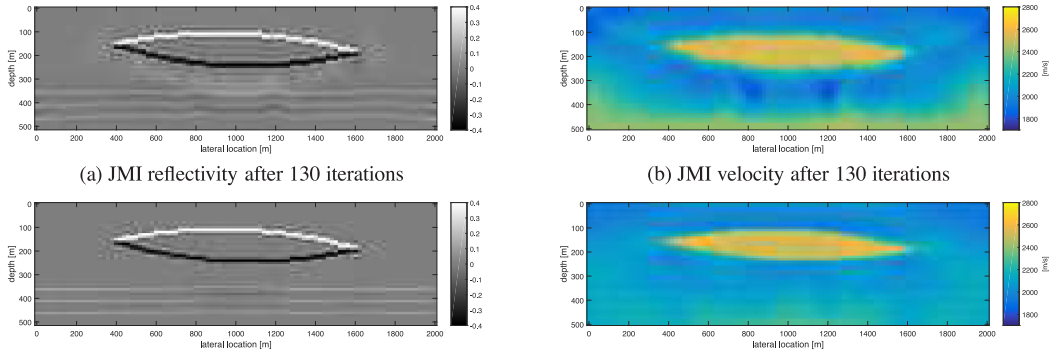

(a) JMI reflectivity after 130 iterations
(b) JMI velocity after 130 iterations
(c) RCJMI reflectivity after 130 iterations
(d) RCJMI velocity after 130 iterations

Figure 7. Estimated reflectivity and velocity models for the first example with frequency schedule III (10–40 Hz). As shown in (c) and (d), accurate reflectivity and velocity can be reconstructed by RCJMI even if the low-frequency components smaller than 10 Hz are absent.

could be obtained, so any imperfection is due to the used inversion algorithm.

4.2 SEG/EAGE salt model

As a more complex and realistic example, a 2D subset of the Society of Exploration Geophysicists/European Association of Geoscientists and Engineers (SEG/EAGE) (Aminzadeh 1997) salt model is used. Rescaling and horizontal resampling for this model are applied in order to reduce computation time. The model contains a salt body, which has high velocity, shown in Figs 10(a) and (b). The receiver and source intervals are 10 and 40 m, respectively.

The frequency schedules I, II and III, described in Table 4–6, are used for the inversions in this example in order to investigate the contribution of the low-frequency components, which are crucial for standard FWI. Table 4 shows that the used frequency bands of seismic data for the inversion consists of four cycles: 1a–3a, 4b–6b, 7c–9c and 10d–13d. This procedure is effective to estimate high-velocity contrasts like salt bodies by both JMI and RCJMI. The maximum offset used for the inversion is 3370 m. Figs 10(c) and (d) show the initial velocity and reflectivity models for JMI and RCJMI, which do not include any information about the salt body. The parameter $\lambda_2 = 10$ is used for RCJMI. The sparse term is not exploited in this example ($\lambda_3 = 0$).

We show the results of JMI using frequency schedule I after 60 iterations in Figs 10(e) and (f) and after 180 iterations in Figs 10(i) and (j). The RCJMI results with frequency schedule I are illustrated in Figs 10(g), (h), (k) and (l), and the RCJMI results using the frequency schedules II and III are shown in Fig. 11. Fig. 12 represents

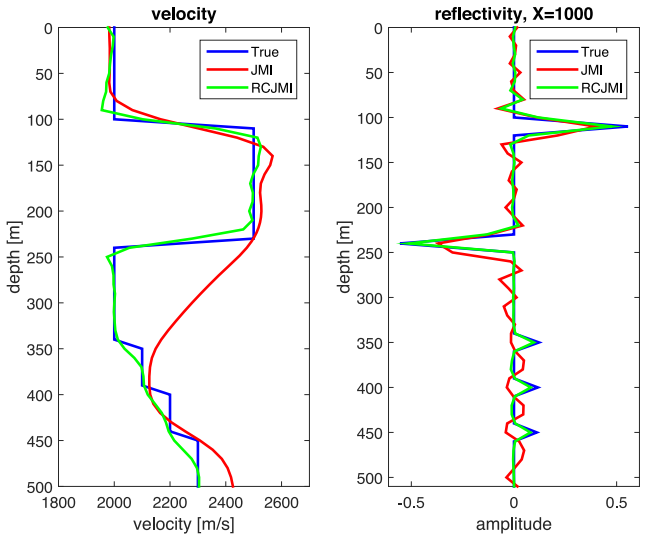

Figure 8. Comparison of the performance after 130 iterations between JMI and RCJMI with frequency schedule I (5–40 Hz) at lateral location x = 1000 m.

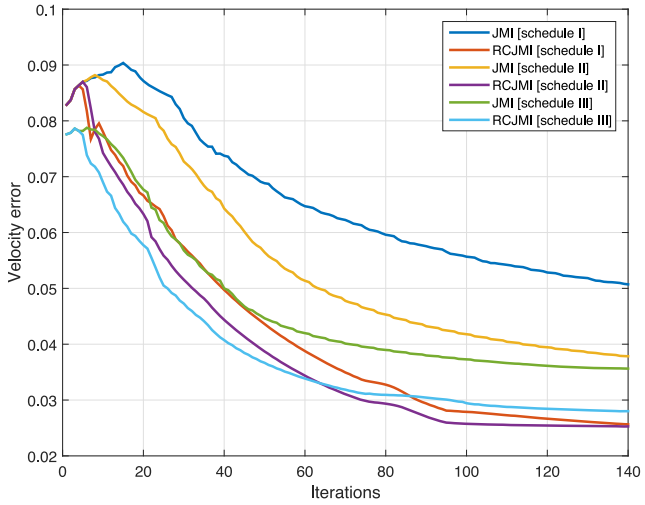

Figure 9. The velocity error c_{error} between the true velocity model and the estimated model from JMI and RCJMI with the frequency schedule I (5–40 Hz), II (5–40 Hz) and III (10–40 Hz). These results demonstrate that the solutions of RCJMI relatively converge to global minima (see red, purple and blue lines).

the iteration dependency of the velocity error c_{error} for JMI and RCJMI.

It can be observed that after 180 iterations JMI does not reconstruct the correct shape of the salt body in the velocity estimation (see Fig. 10j). However, RCJMI gives the accurate shape of the salt body owing to its reflectivity-constrained velocity estimation in an early iteration stage (see Fig. 10l). As a result, the reflectivity image is clear (see Fig. 10k), although the depth of the imaged reflectivity below the salt body is slightly inaccurate due to the overestimated velocity under the salt body. As shown in Figs 11 and 12, both the velocity and reflectivity distributions are effectively estimated without accurate initial models and low-frequency components of the observed seismic data. A close inspection of Fig. 12 shows that the results without the low-frequency components up to 10Hz, surprisingly enough, show an improved performance in terms of the velocity estimation in RCJMI.

4.3 Field data example

Finally, we test our proposed method for a 2D field data provided by Statoil. The data was acquired by a streamer survey in the North Sea, in the Vøring area, offshore Norway. The receiver and source intervals used in our process are 25 m and 50 m, respectively. The direct wave and the surface-related multiples have been removed, and receiver deghosting was applied.

The source wavelet used for JMI and RCJMI is estimated from the surface-related multiples using the so-called estimation of primaries by sparse inversion (EPSI) process (van Groenestijn & Verschuur 2009). As shown in Table 7 and 8, 5-40 Hz and 7-40 Hz of the seismic data are prepared for JMI and RCJMI, respectively because it was demonstrated that RCJMI is not sensitive to the existence of low-frequency components in the above synthetic examples. The maximum offset used for the inversion is 2500 m. As the initial velocity model, a simple 1D velocity function shown in Fig. 13(b) has been chosen. The parameter λ_2=2 is used for RCJMI. The sparsity term is not exploited in this example (λ_3=0).

Figs 13(c) and (d) show the reflectivity and velocity estimated by JMI after 85 iterations and Figs 13(e) and (f) illustrate the migrated reflectivity and reconstructed velocity after 85 RCJMI iterations. To compare the detail of the estimated velocity and reflectivity models, we show the models in the depth levels 1500-2400 m in Fig. 14. As illustrated in Figs 14(a) and (b), the velocity reconstructed by RCJMI has high resolution and matches the structure of the estimated reflectivity well, although the lateral variation in the high velocity layer produced by JMI may be somewhat unlikely in the light of the estimated reflectivity (see the part of the lateral locations 2000-3000 m and the depth levels 1700–2000 m in Fig. 14c). Note that the difference of reflectivity estimated by between JMI and RCJMI is not large because the velocity variation in this example is relatively small.

5 DISCUSSION

5.1 Computational cost

The extra computational cost of our proposed constraint is small. When the computational time of JMI and RCJMI for 10 iterations in the first example with the 2D lense-shaped model is measured, the increase of the computational time by RCJMI is 1.0 per cent per iteration on average. Therefore, this constraint does not require large extra computational cost.

5.2 Density variations

Our proposed algorithm assumes that for the constraint calculation the density of the subsurface is constant, as stated in eq. (17). Since density variations are generally smaller than velocity variations, this assumption would be realistic. However, density variations can be simply included in the constraint if a well-known empirical relation, so-called Gardner's relation (Gardner *et al.* 1974), in rock physics is used, which is given by:

$$\rho(x,z) = Ac(x,z)^B, \tag{32}$$

where $A, B \in \mathbb{R}^+$ represent the parameters for fitting. If velocity c and density ρ are measured in m/s and g/cm^3, respectively, the observation that taking $A = 0.31$ and $B = 0.25$ gives a good fit for typical sediments is reported in (Gardner *et al.* 1974). A modified reflectivity can be represented by the following equation instead of

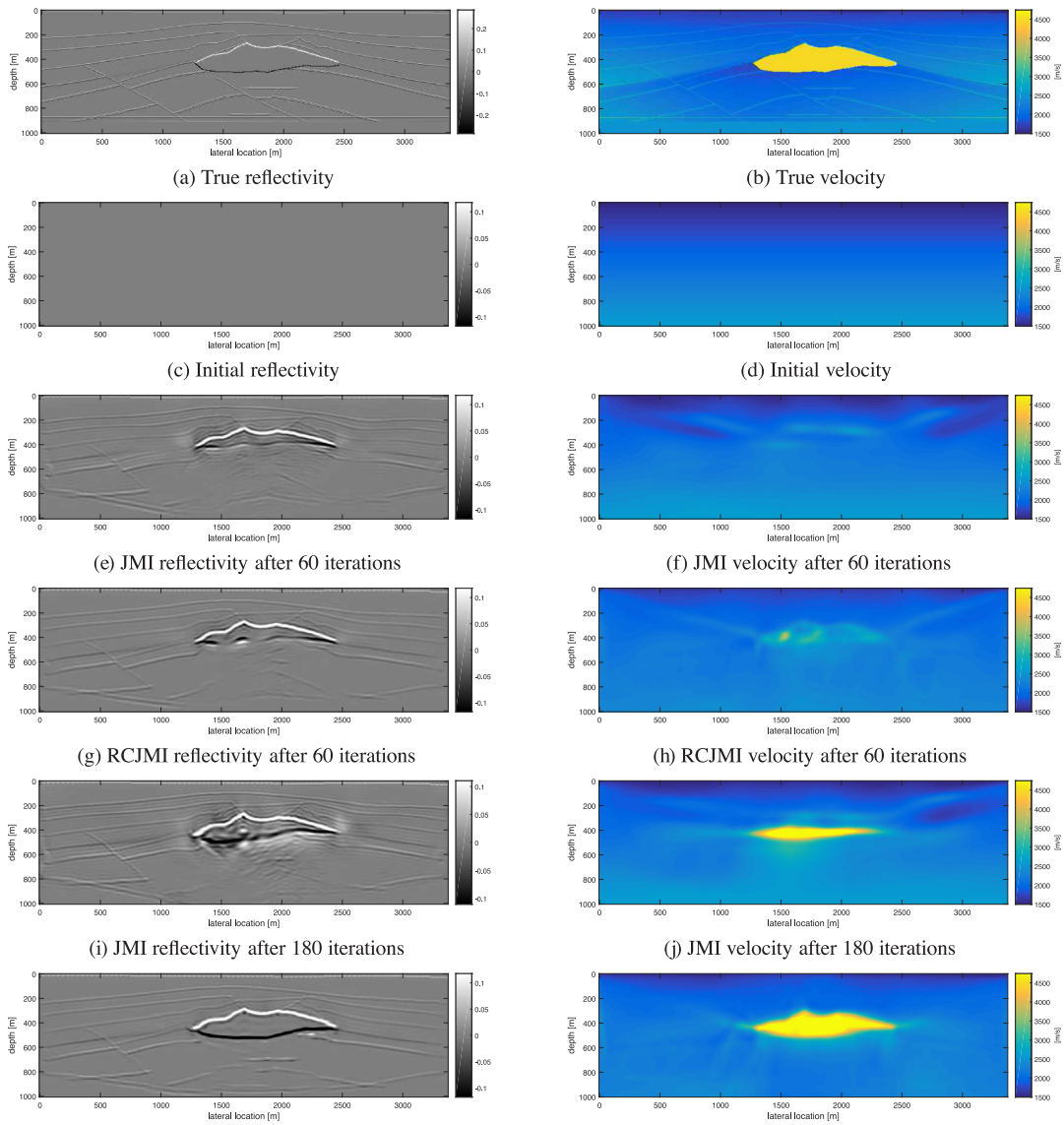

(a) True reflectivity (b) True velocity

(c) Initial reflectivity (d) Initial velocity

(e) JMI reflectivity after 60 iterations (f) JMI velocity after 60 iterations

(g) RCJMI reflectivity after 60 iterations (h) RCJMI velocity after 60 iterations

(i) JMI reflectivity after 180 iterations (j) JMI velocity after 180 iterations

(k) RCJMI reflectivity after 180 iterations (l) RCJMI velocity after 180 iterations

Figure 10. Reflectivity and velocity models in the second example with frequency schedule I (5–40 Hz).

Table 4. The frequency schedule I for JMI and RCJMI in the SEG/EAGE salt model example.

Order	Frequency (Hz)	No. of iterations
1a	5–10	10
2a	5–25	10
3a	5–40	10
4b	5–10	10
5b	5–25	10
6b	5–40	10
7c	5–10	10
8c	5–25	10
9c	5–40	10
10d	5–10	12
11d	5–20	12
12d	5–30	10
13d	5–40	56
		Total 180

Table 5. The frequency schedule II for RCJMI in the SEG/EAGE salt model example.

Order	Frequency (Hz)	No. of iterations
1a	7–11	10
2a	7–25.5	10
3a	7–40	10
4b	7–11	10
5b	7–25.5	10
6b	7–40	10
7c	7–11	10
8c	7–25.5	10
9c	7–40	10
10d	7–11	12
11d	7–20.6	12
12d	7–30.3	10
13d	7–40	56
		Total 180

Table 6. The frequency schedule III for RCJMI in the SEG/EAGE salt model example.

Order	Frequency (Hz)	No. of iterations
1a	10–14	10
2a	10–27	10
3a	10–40	10
4b	10–14	10
5b	10–27	10
6b	10–40	10
7c	10–14	10
8c	10–27	10
9c	10–40	10
10d	10–14	12
11d	10–22.7	12
12d	10–31.3	10
13d	10–40	56
		Total 180

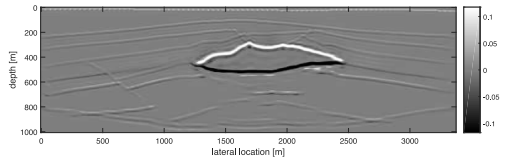

(a) RCJMI reflectivity with frequency schedule II (7-40 Hz)

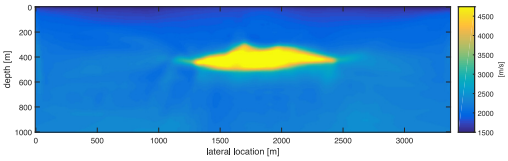

(b) RCJMI velocity with frequency schedule II (7-40 Hz)

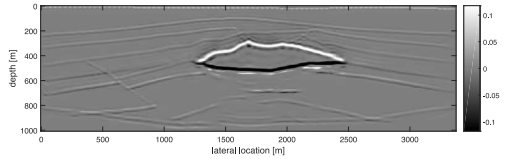

(c) RCJMI reflectivity with frequency schedule III (10-40 Hz)

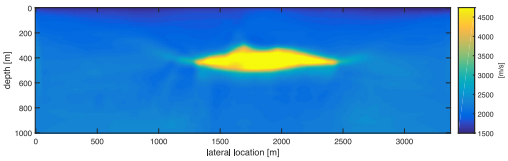

(d) RCJMI velocity with frequency schedule III (10-40 Hz)

Figure 11. RCJMI reflectivity and velocity models after 180 iterations with frequency schedules II (7–40 Hz) and III (10–40 Hz).

eq. (16):

$$r(x, z_{n+1}) = \frac{Ac(x, z_{n+1})^{B+1} - Ac(x, z_n)^{B+1}}{Ac(x, z_{n+1})^{B+1} + Ac(x, z_n)^{B+1}} = \frac{c(x, z_{n+1})^{B+1} - c(x, z_n)^{B+1}}{c(x, z_{n+1})^{B+1} + c(x, z_n)^{B+1}}. \quad (33)$$

Here, using $\zeta(x, z) \equiv c(x, z)^{B+1}$, we can derive an approximation:

$$r(x, z_{n+1}) \sim \frac{\Delta\zeta}{\Delta z} \times \text{const.}, \quad (34)$$

where $\Delta\zeta \equiv \zeta(x, z_{n+1}) - \zeta(x, z_n)$. Since this eq. (34) has a similarity with eq. (18), a similar constraint can be formulated by defining $r_{\text{constr}}(x, z_{n+1}) \equiv \partial\zeta/\partial z$ and $r_{\text{res}}(x, z) \equiv r(x, z) - \Lambda r_{\text{constr}}(x, z)$. The

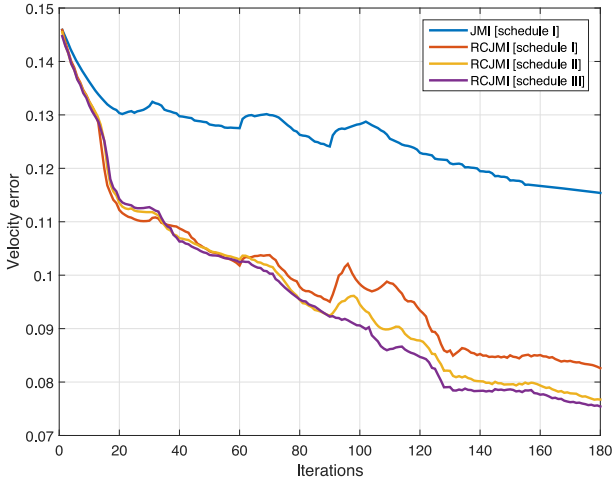

Figure 12. The velocity error c_{error} between the true velocity model and the estimated model from JMI and RCJMI using frequency schedule I (5-40 Hz), II (7-40 Hz), and III (10-40 Hz). Compared with JMI, RCJMI remarkably reduces the velocity error independently of the existence of low-frequency components.

Table 7. The frequency schedule for JMI in the field data example.

Order	Frequency (Hz)	No. of iterations
1a	5–10	10
2a	5–20	10
3a	5–30	10
4a	5–40	5
5b	5–20	10
6b	5–30	10
7b	5–40	5
8c	5–20	10
9c	5–30	10
10c	5–40	5
		Total 85

Table 8. The frequency schedule for RCJMI in the field data example.

Order	Frequency (Hz)	No. of iterations
1a	7–11	10
2a	7–20.6	10
3a	7–30.3	10
4a	7–40	5
5b	7–20.6	10
6b	7–30.3	10
7b	7–40	5
8c	7–20.6	10
9c	7–30.3	10
10c	7–40	5
		Total 85

gradient for velocity update described in eq. (28) is replaced by:

$$\nabla J_{2,c}(x, z) = \lambda_2[\zeta_{\text{res}}(x, z)]^{1/(B+1)}, \quad (35)$$

with

$$\zeta_{\text{res}}(x, z) \equiv \int_{z_0}^{z} r_{\text{res}}(x, z')dz'. \quad (36)$$

Hence, this extension of the proposed constraint is capable of dealing with density variations by giving a parameter B. Note again that since Gardner's relation is an empirical relation, this extension does not take account of any physics theory. Finally, note that this relation

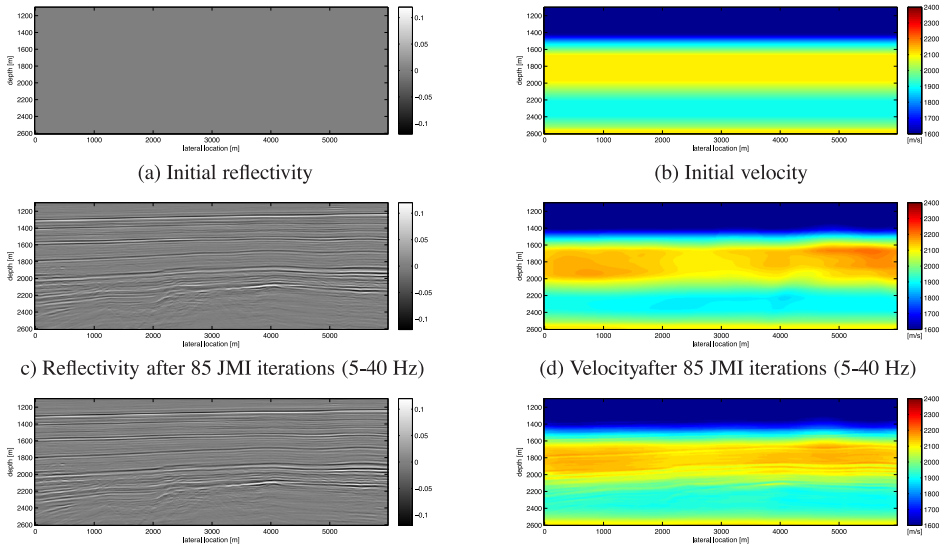

(a) Initial reflectivity

(b) Initial velocity

c) Reflectivity after 85 JMI iterations (5-40 Hz)

(d) Velocityafter 85 JMI iterations (5-40 Hz)

(e) Reflectivity after 85 RCJMI iterations (7-40 Hz)

(f) Velocity after 85 RCJMI iterations (7-40 Hz)

Figure 13. Estimated reflectivity and velocity models in the field data example.

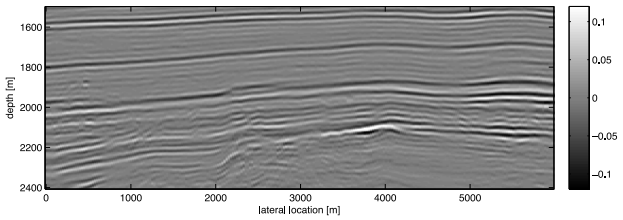

(a) Reflectivity after 85 RCJMI iterations (7-40 Hz)

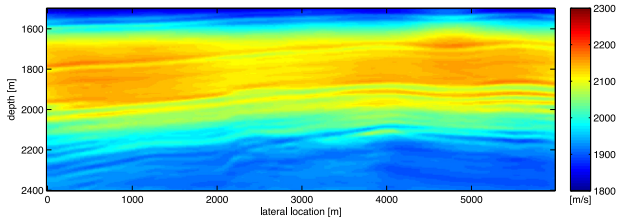

(b) Velocity after 85 RCJMI iterations (7-40 Hz)

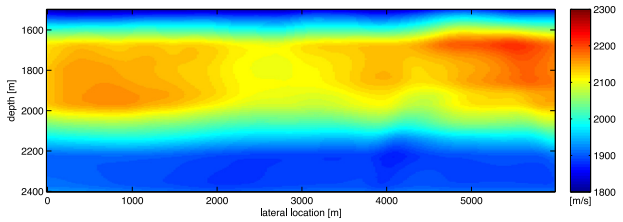

(c) Velocity after 85 JMI iterations (5-40 Hz)

Figure 14. Estimated reflectivity and velocity models for depth levels 1500-2400 m. It is found that the RCJMI velocity has a better correspondence to its reflectivity.

is only used in the constraint for updating the velocity; the forward modelling process within JMI does not rely on this assumption.

6 CONCLUSIONS

We propose an algorithm for reflectivity-constrained velocity estimation to improve its accuracy through a novel velocity update process utilizing the inverted reflectivity in each iteration. This algorithm does not require any prior information of the subsurface and large extra computational costs, such as the calculation of so-called Hessian matrices.

The numerical and field data examples demonstrate that the proposed reflectivity-constrained JMI algorithm enables us to largely improve the automatic velocity estimation, even in the case of high-velocity contrasts, without accurate initial models, although the final velocity model is not perfect yet probably due to the typical velocity-depth ambiguities. The reflectivity distributions are also improved owing the accurate velocity. Moreover, the experiments showed that the performance of the algorithm was not sensitive to the existence of the used low-frequency components of observed data and to the used frequency schedule for the inversion.

ACKNOWLEDGEMENTS

The authors thank Statoil for providing the field data. They also acknowledge the sponsors of the Delphi consortium for their support. Shogo Masaya would like to thank INPEX for the financial support of his study at Delft University of Technology.

REFERENCES

Aminzadeh , F., Brac, J. & Kunz, T., 1997. *3D salt and Overthrust models,* SEG/EAGE Modeling Series, No. 1, Distribution CD of Salt and Overthrust models, SEG Book Series Tulsa, Oklahoma.

Berkhout, A.J., 1982. *Seismic Migration, Imaging of Acoustic Energy by Wave Field Extrapolation, A: Theoretical Aspects,* 2nd edn, Elsevier.

Berkhout, A.J., 2012. Combining full wavefield migration and full waveform inversion, a glance into the future of seismic processing, *Geophysics,* **77,** S43–S50.

Berkhout, A.J., 2014a. Review paper: an outlook on the future of seismic imaging, part I: forward and reverse modelling, *Geophys. Prospect.,* **62,** 911–930.

Berkhout, A.J., 2014b. Review paper: an outlook on the future of seismic imaging, part III: joint migration inversion, *Geophys. Prospect.,* **62,** 950–971.
Berkhout, A.J. & Verschuur, D.J., 2011. Full wavefield migration, utilizing surface and internal multiple scattering, *Soc. Expl. Geophys., Expanded abstracts,* **77**(2), 3212–3216.
Biondi, B. & Almomin, A., 2012. Tomographic full waveform inversion (TFWI) by combining full waveform inversion with wave equation velocity analysis, *Soc. Expl. Geophys., Expanded abstracts,* **32**(9), 1074–1080.
Biondi, B. & Symes, W., 2004. Angle domain common-image gathers for migration velocity analysis by wavefield continuation imaging, *Geophysics,* **69,** 1283–1298.
Bremmer, H., 1951. The WKB approximation as the first term of a geometric-optical series, *Commun. Pure appl. Math,* **4,** 105–115.
Davydenko, M. & Verschuur, D.J., 2017. Full-wavefield migration: using surface and internal multiples in imaging, *Geophys. Prospect.,* **65,** 7–21.
Esser, E., Guasch, L., van Leeuwen, T., Aravkin, A.Y. & Herrmann, F.J., 2015. Total variation regularization strategies in full waveform inversion for improving robustness to noise, limited data and poor initializations, Technical Report, TR-EOAS-2015-5.
Gardner, G.H.F., Gardner, L.W. & Gregory, A.R., 1974. Formation velocity and density – the diagnostic basis for stratigraphic traps, *Geophysics,* **39,** 770–780.
Gazdag, J., 1978. Wave equation migration with the phase-shift method, *Geophysics,* **43,** 1342–1351.
Goldstein, T. & Osher, S., 2009. The split bregman method for L1-regularized problems, *SIAM J. Imagi.Sci.,* **2,** 323–343.
Ji, S., Huang, T., Fu, K. & Li, Z., 2011. Dirty salt velocity inversion: the road to a clearer subsalt image, *Geophysics,* **76,** WB169–WB174.
Kinneging, N.K., Budejicky, V., Wapenaar, C.P.A. & Berkhout, A.J., 1989. Efficient 2D and 3D shot record redatuming, *Geophys. Prospect.,* **37,** 493–530.
Liu, Z. & Bleistein, N., 1995. Migration velocity analysis: theory and an iterative algorithm, *Geophysics,* **60,** 142–153.
Maciel, J.S., Costa, J.C. & Verschuur, D.J., 2015. Enhancing resolution in imaging-based velocity estimation using morphological operators, *Soc. Expl. Geophys., Expanded abstracts,* 5228–5232.
Masaya, S. & Verschuur, D.J., 2016. Joint migration inversion based on reflectivity-constrained velocity estimation, *Soc. Expl. Geophys., Expanded abstracts,* 5379–5383.
Mathewson, J.C., Evans, D., Leone, C., Leathard, M., Dangerfield, J. & Tonning, S.A., 2012. Improved imaging and resolution of overburden heterogeneity by combining amplitude inversion with tomography, *Soc. Expl. Geophys., Expanded abstracts,* 1–5.
Qiu, L., Zou, K., Valenciano, A. & Chemingui, N., 2016. Full waveform inversion with steerable variation regularization, *Soc. Expl. Geophys., Expanded abstracts,* 1174–1178.
Sacchi, M.D., Ulrych, T.J. & Walker, C.J., 1998. Interpolation and extrapolation using a high-resolution discrete Fourier transform, *IEEE Trans. Signal Process.,* **46,** 31–38.
Sava, P. & Biondi, B., 2004. Wave equation migration velocity analysis. I. Theory, *Geophys. Prospect.,* **52,** 593–606.
Staal, X.R., 2015. Combined imaging and velocity estimation by joint migration inversion, *PhD thesis,* Delft University of Technology.
Staal, X.R. & Verschuur, D.J., 2013. Joint migration inversion, imaging including all multiples with automatic velocity update, *Eur. Assoc. Geosci. Eng., Expanded abstracts,* Tu-02-16, 4pp.
Staal, X.R., Verschuur, D.J. & Berkhout, A.J., 2014. Robust velocity estimation by joint migration inversion, *Eur. Assoc. Geosci. Eng., Expanded abstracts,* 4290–4295.
Tarantola, A., 1984. Inversion of seismic reflection data in the acoustic approximation, *Geophysics,* **49,** 1259–1266.
van Groenestijn, G.J.A. & Verschuur, D.J., 2009. Estimating primaries by sparse inversion and application to near-offset data reconstruction, *Geophysics,* **74,** A23–A28.
van Leeuwen, T. & Herrmann, F.J., 2016. A penalty method for PDE-constrained optimization in inverse problems, *Inverse Probl.,* **32,** 1–26.
Verschuur, D.J., Staal, X.R. & Berkhout, A.J., 2016. Joint migration inversion: simultaneous determination of velocity fields and depth images using all orders of scattering, *Leading Edge,* **35,** 1037–1046.
Virieux, J. & Operto, S., 2009. An overview of full-waveform inversion in exploration geophysics, *Geophysics,* **74,** WCC127–WCC152.
Warner, M. & Guasch, L., 2016. Adaptive waveform inversion: theory, *Geophysics,* **81,** R429–R445.

APPENDIX A: REFLECTIVITY AND VELOCITY UPDATES BY JMI

This section derives the update rules for JMI. If we assume that reflection coefficients are angle and frequency independent and the subsurface wave conversion is small, we can obtain the following approximations:

$$\mathbf{R}(z_n) = \mathbf{R}^{\cup}(z_n) = -\mathbf{R}^{\cap}(z_n), \tag{A1}$$

$$\delta\mathbf{T}^{+}(z_n) = \mathbf{R}(z_n), \tag{A2}$$

$$\delta\mathbf{T}^{-}(z_n) = -\mathbf{R}(z_n), \tag{A3}$$

where $\mathbf{R}(z_n)$ and $\mathbf{T}(z_n)$ are diagonal matrices at depth level z_n with scalar reflectivity $r(x, z_n)$ and transmission $t(x, z_n)$, respectively, along their diagonals.

A1 Reflectivity update

Calculation of their gradients is required to update the reflectivity and velocity models by the gradient descent scheme. We can derive the gradient for the reflectivity update:

$$\begin{aligned}\nabla\vec{J}_r(z_n) = diag\Bigg(\sum_{\xi}^{N_s}\sum_{f}^{N_\omega}[\underline{\mathbf{W}}_i^{-}(z_0;z_n,\omega_f)]^H\vec{E}_i(z_0,x_{s,\xi},\omega_f)\\ [\vec{P}_i^{+}(z_n,x_{s,\xi},\omega_f)]^H\Bigg) - diag\Bigg(\sum_{\xi}^{N_s}\sum_{f}^{N_\omega}\Bigg[\sum_{m=n+1}^{M}\\ [\underline{\mathbf{W}}_i^{+}(z_m;z_n,\omega_f)]^H\mathbf{R}(z_m)\underline{\mathbf{W}}_i^{-}(z_0;z_m,\omega_f)\Bigg]^H\\ \vec{E}_i(z_0,x_{s,\xi},\omega_f)[\vec{P}_{i-1}^{-}(z_n,x_{s,\xi},\omega_f)]^H\Bigg),\end{aligned} \tag{A4}$$

with

$$\vec{E}_i(z_0,x_{s,\xi},\omega_f) \equiv \vec{P}_{obs}^{-}(z_0,x_{s,\xi},\omega_f) - \vec{P}_{mod,i}^{-}(z_0,x_{s,\xi},\omega_f), \tag{A5}$$

where $\vec{E}_i(z_0,x_{s,\xi},\omega_f)$ represents the residual between observed and modelled shot data at ith roundtrip and H indicates the Hermitian conjugate. Note that the first term of the RHS in eq. (A4) means the cross-correlation between the back-propagated upgoing wavefield for the residual and the forward modelled downgoing wavefield. The second term indicates the cross-correlation between the back-propagated downgoing wavefield for the residual and the forward modelled upgoing wavefield. Thus, eq. (A4) can be interpreted as the reflectivity image of the residual data. The wavefield perturbation can be obtained from the gradient as follows:

$$\begin{aligned}\Delta\vec{P}_{J,r}^{-}(z_0,x_{s,\xi},\omega_f) = \sum_{n=1}^{M}\underline{\mathbf{W}}_i^{-}(z_0;z_n,\omega_f)\nabla\mathbf{J}_r(z_n)\\ \vec{P}_i^{+}(z_n,x_{s,\xi},\omega_f),\end{aligned} \tag{A6}$$

where $\nabla \mathbf{J}_r(z_n)$ is a square matrix with the gradient $\nabla \vec{J}_r(z_n)$ along its diagonal. A scale factor to adjust the reflectivity update in each iteration is defined by:

$$\alpha_r = \frac{\sum_{\xi}^{N_s} \sum_{f}^{N_\omega} [\Delta \vec{P}^-_{J,r}(z_0, x_{s,\xi}, \omega_f)]^H \vec{E}_i(z_0, x_{s,\xi}, \omega_f)}{\sum_{\xi}^{N_s} \sum_{f}^{N_\omega} \|\Delta \vec{P}^-_{J,r}(z_0, x_{s,\xi}, \omega_f)\|^2}. \tag{A7}$$

Finally, we can update the reflectivity model as follows:

$$r^{(k+1)}(x, z) = r^{(k)}(x, z) + \alpha_r \nabla J_r(x, z), \tag{A8}$$

where $\nabla J_r(x, z)$ are the diagonal elements of $\nabla \mathbf{J}_r(z_n)$. Note that in the above description, unlike the formulation of Berkhout (2014b), the transmission operators have been included in the $\mathbf{W}$'s, yielding the $\underline{\mathbf{W}}$'s, providing a somewhat more accurate gradient.

A2 Slowness update

The velocity updating procedure is similar to the reflectivity update. To keep the notation similar, we describe the procedure to update the slowness ($\sigma = 1/c$) model instead of the velocity model (Staal 2015).

First, we derive a linearized relationship between the propagation operators and the slowness model by introducing their perturbations. The propagation operators are based on the phase-shift operator in the wavenumber domain:

$$\tilde{w}(k_x, \omega) = e^{-jk_z \Delta z}, \tag{A9}$$

with

$$k_z(\sigma) = \sqrt{\omega^2 \sigma^2 - k_x^2}. \tag{A10}$$

Using their perturbations, we can obtain the following linearized equation:

$$\begin{aligned} \Delta \tilde{w} = \tilde{w}_{\text{new}} - \tilde{w}_{\text{old}} &\approx \left[\frac{\partial \tilde{w}}{\partial \sigma}\right]_{\sigma_{\text{old}}} \Delta\sigma \\ &= -j\omega \left[\frac{k}{k_z}\right]_{\sigma_{\text{old}}} \tilde{w}_{\text{old}} \Delta\sigma, \end{aligned} \tag{A11}$$

where $\tilde{w}_{\text{new}}$ is the operator in an updated slowness model σ_{new} and $\tilde{w}_{\text{old}}$ is the operator in the current slowness model σ_{old}. Then, an operator $\mathbf{L}$, which is similar to the propagation operators in eq. (9), is defined by:

$$\vec{L}_j(z_m; z_n) = \mathcal{F}_x^{-1}\left[-j\omega\Delta z \left[\frac{k_z^* k}{|k_z|^2 + \epsilon}\right]_{\sigma_{\text{old}}} e^{-jk_z \Delta z} e^{-jk_x x_j}\right], \tag{A12}$$

where ϵ is a small stabilization parameter and $*$ indicates complex conjugate. Therefore, we can derive a linearized relationship between the propagation operators and the slowness model:

$$\Delta \mathbf{W}^-(z_{n+1}; z_n) \approx \mathbf{L}^+(z_{n+1}; z_n) \Delta\sigma(z_n), \tag{A13}$$

$$\Delta \mathbf{W}^+(z_n; z_{n+1}) \approx \Delta\sigma(z_n) \mathbf{L}^-(z_n; z_{n+1}), \tag{A14}$$

where $\Delta\sigma(z_n)$ is a diagonal matrix with the slowness updates $\Delta\sigma(x, z_n)$ along its diagonal. An operator $\mathbf{L}^+(z_{n+1}; z_n)$ is defined as $\mathbf{L}^+(z_{n+1}; z_n) = [\mathbf{L}^-(z_n; z_{n+1})]^T$.

We calculate the update direction for the propagation operators:

$$\begin{aligned} \Delta \mathbf{W}^-(z_n; z_{n+1}, \omega_f) = &\sum_{\xi}^{N_s} [\mathbf{V}_i^-(z_0; z_n, \omega_f)]^H \\ &\vec{E}_i(z_0, x_{s,\xi}, \omega_f) [\vec{Q}_i^-(z_{n+1}, x_{s,\xi}, \omega_f)]^H, \end{aligned} \tag{A15}$$

$$\begin{aligned} \Delta \mathbf{W}^+(z_{n+1}; z_n, \omega_f) = &\sum_{\xi}^{N_s} [\mathbf{V}_i^{\cup}(z_0; z_{n+1}, \omega_f)]^H \\ &\vec{E}_i(z_0, x_{s,\xi}, \omega_f) [\vec{Q}_i^+(z_n, x_{s,\xi}, \omega_f)]^H, \end{aligned} \tag{A16}$$

with

$$\mathbf{V}_i^-(z_0; z_n, \omega_f) \equiv \underline{\mathbf{W}}_i^-(z_0; z_n, \omega_f)[\mathbf{I} - \mathbf{R}_i(z_n)], \tag{A17}$$

$$\begin{aligned} \mathbf{V}_i^{\cup}(z_0; z_{n+1}, \omega_f) \equiv &\underline{\mathbf{W}}_i^-(z_0; z_n, \omega_f) \mathbf{R}_i(z_n) \\ &+ \sum_{m=n+1}^{M} \underline{\mathbf{W}}_i^-(z_0; z_m, \omega_f) \mathbf{R}_i(z_m) \\ &\underline{\mathbf{W}}_i^+(z_m; z_n, \omega_f)[\mathbf{I} + \mathbf{R}_i(z_n)], \end{aligned} \tag{A18}$$

and

$$\vec{Q}_i^+(z_n) = [\mathbf{I} + \mathbf{R}_i(z_n)] \vec{P}_i^+(z_n) - \mathbf{R}_i(z_n) \vec{P}_{i-1}^-(z_n), \tag{A19}$$

$$\vec{Q}_i^-(z_n) = [\mathbf{I} - \mathbf{R}_i(z_n)] \vec{P}_i^-(z_n) + \mathbf{R}_i(z_n) \vec{P}_i^+(z_n), \tag{A20}$$

where i represents the number of roundtrips. Hence, we can calculate the gradient for the slowness update:

$$\begin{aligned} \nabla \vec{J}_\sigma(z_n) = diag\Bigg\{ &\sum_{f}^{N_\omega} \Delta \mathbf{W}^-(z_n; z_{n+1}, \omega_f) \\ &[\mathbf{L}^-(z_n; z_{n+1}, \omega_f)]^H \Bigg\} + diag\Bigg\{ \sum_{f}^{N_\omega} \\ &[\mathbf{L}^+(z_{n+1}; z_n, \omega_f)]^H \Delta \mathbf{W}^+(z_{n+1}; z_n, \omega_f) \Bigg\}. \end{aligned} \tag{A21}$$

The wavefield perturbation can be obtained from the gradient as follows:

$$\begin{aligned} \Delta \vec{P}^-_{J,\sigma}(z_0, x_{s,\xi}, \omega_f) = &\sum_{n=1}^{M} \mathbf{V}_i^-(z_0; z_n, \omega_f) \nabla \mathbf{J}_\sigma(z_n) \\ &\mathbf{L}^-(z_n; z_{n+1}, \omega_f) \vec{Q}_i^-(z_{n+1}, x_{s,\xi}, \omega_f) \\ &+ \sum_{n=1}^{M} \mathbf{V}_i^{\cup}(z_0; z_{n+1}, \omega_f) \mathbf{L}^+(z_{n+1}; z_n, \omega_f) \\ &\nabla \mathbf{J}_\sigma(z_n) \vec{Q}_i^+(z_n, x_{s,\xi}, \omega_f), \end{aligned} \tag{A22}$$

where $\nabla \mathbf{J}_\sigma(z_n)$ indicates a square matrix with the gradient $\nabla \vec{J}_\sigma(z_n)$ along its diagonal. On the basis of the wavefield perturbation, a scale factor for the slowness update in each iteration is defined by:

$$\alpha_\sigma = \frac{\sum_{\xi}^{N_s} \sum_{f}^{N_\omega} [\Delta \vec{P}^-_{J,\sigma}(z_0, x_{s,\xi}, \omega_f)]^H \vec{E}(z_0, x_{s,\xi}, \omega_f)}{\sum_{\xi}^{N_s} \sum_{f}^{N_\omega} \|\Delta \vec{P}^-_{J,\sigma}(z_0, x_{s,\xi}, \omega_f)\|^2}. \tag{A23}$$

Finally, we can update the slowness model:

$$\sigma^{(k+1)}(x, z) = \sigma^{(k)}(x, z) + \alpha_\sigma \nabla J_\sigma(x, z). \tag{A24}$$